frontiers in Chemistry

ORIGINAL RESEARCH
published: 27 January 2022
doi: 10.3389/fchem.2022.837915

Epitaxial Growth of Flower-Like MoS_2 on One-Dimensional Nickel Titanate Nanofibers: A "Sweet Spot" for Efficient Photoreduction of Carbon Dioxide

Haritham Khan[1], *Suhee Kang*[2], *Hazina Charles*[1] *and Caroline Sunyong Lee*[1]*

[1]Department of Materials and Chemical Engineering, Hanyang University, Ansan, South Korea, [2]POSCO Chemical, Sandan-gil, Jeonui-myeon, Pohang, South Korea

Herein, a full spectrum-induced hybrid structure consisting of one-dimensional nickel titanate ($NiTiO_3$) nanofibers (NFs) decorated by petal-like molybdenum disulfide (MoS_2) particles was designed through a facile hydrothermal method. The key parameters for tailoring the morphology and chemical, surface, and interfacial properties of the heterostructure were identified for efficient and selective conversion of CO_2 into valuable chemicals. Introducing MoS_2 layers onto $NiTiO_3$ NFs provided superior CO_2 conversion with significantly higher yields. The optimized hybrid structure produced CO and CH_4 yields of 130 and 55 μmol g^{-1} h^{-1}, respectively, which are 3.8- and 3.6-times higher than those from pristine $NiTiO_3$ nanofibers (34 and 15 μmol g^{-1} h^{-1}, respectively) and 3.6- and 5.5-times higher than those from pristine MoS_2 (37 and 10 μmol g^{-1} h^{-1}, respectively). This improved performance was attributed to efficient absorption of a wider spectrum of light and efficient transfer of electrons across the heterojunction. Effective charge separation and reduced charge carrier recombination were confirmed by photoluminescence and impedance measurements. The performance may also be partly due to enhanced hydrophobicity of the hierarchical surfaces due to MoS_2 growth. This strategy contributes to the rational design of perovskite-based photocatalysts for CO_2 reduction.

Keywords: artificial photosynthesis, CO_2 reduction, hydrophobic nature, Mos_2, $NiTiO_3$, electrospining

OPEN ACCESS

Edited by:
Pengyu Dong,
Yancheng Institute of Technology, China

Reviewed by:
Shijie Li,
Zhejiang Ocean University, China
Zeai Huang,
Southwest Petroleum University, China

***Correspondence:**
Caroline Sunyong Lee
sunyonglee@hanyang.ac.kr

Specialty section:
This article was submitted to Catalysis and Photocatalysis, a section of the journal Frontiers in Chemistry

Received: *17 December 2021*
Accepted: *10 January 2022*
Published: *27 January 2022*

Citation:
Khan H, Kang S, Charles H and Lee CS (2022) Epitaxial Growth of Flower-Like MoS_2 on One-Dimensional Nickel Titanate Nanofibers: A "Sweet Spot" for Efficient Photoreduction of Carbon Dioxide. Front. Chem. 10:837915. doi: 10.3389/fchem.2022.837915

INTRODUCTION

Global warming due to excessive emission of anthropogenic carbon dioxide has become an increasingly serious environmental concern. It is therefore imperative to develop strategies to mitigate CO_2 emissions. Exhaustive research has examined sustainable technologies for CO_2 reduction (Thompson et al., 2020). Photocatalytic CO_2 reduction is of particular interest, to produce chemical fuels via solar energy conversion, but the activity, stability, and selectivity of the products are strongly dependent on the efficiencies of light-harvesting, charge migration, and surface reactions (Li et al., 2019b).

Nickel titanium trioxide (nickel titanate; $NiTiO_3$), a member of the Ti-based perovskite oxide group, has recently received attention due to its photocatalytic activity in visible light (2.1–2.9 eV)

(He et al., 2016; Pham and Shin, 2020). $NiTiO_3$, with its advantage of octahedrally coordinated Ni and Ti, has a narrow bandgap contrary to that of traditional ultraviolet (UV)-active photocatalysts. Zeng et al. (Zeng et al., 2018) reported nontoxic and low-cost perovskites having more suitable energy bands for CO_2 reduction and greater stability against photocorrosion. However, recombination of charge carriers occurred when they were used as individual photocatalysts. Effect of heterostructure formation in the semiconductor-based photocatalysts has gained much interest. Semiconductor-based photo-catalysts showed dramatic reduction in the recombination rates with heterostructure formation which are widely applied in antibiotic removal (Li et al., 2021; 2022a), pharmaceutical wastewater treatment (Li et al., 2020b), and toxicity analysis applications (Li et al., 2022b; Wang et al., 2022). Therefore, a composite photocatalyst was required to effectively reduce recombination rates.

Two-dimensional (2D) transition-metal dichalcogenides (TMDs) are another emerging group of materials that show promise because of their unique nanoflower morphology, consisting of layered structures with thin open edges (Chen et al., 2017; Zhang et al., 2020; Gan et al., 2021). TMDs have improved light absorption and charge separation, and hence various catalytic properties. Unlike H_2 evolution, water treatment, and water splitting, research on CO_2 reduction performance is still in its infancy. Molybdenum disulfide (MoS_2; ~1.3 eV) is the most frequently used TMD having a graphite-like 2D structure. Due to its facile synthesis and cost-effectiveness, MoS_2 is regarded as an ideal substitute for noble metals in the context of photocatalytic H_2 evolution. MoS_2 has three polytypic structures, with the hexagonal 2H and octahedral 1T phases being the most common. The metastable 1T phase, which is active on basal and edge planes, unlike the 2H phase, has interesting chemical and physical properties but its synthesis is challenging (Asadi et al., 2014; Li et al., 2018; Li et al., 2020a; Thomas et al., 2021).

The rational design and preparation of dissimilar dimensional materials (e.g.,1D/2D) has therefore been extensively investigated for use as heterogeneous photocatalysts (Peng et al., 2017; Su et al., 2018; Xu et al., 2018; Li et al., 2020a; Qu et al., 2020). The 1D materials possess distinct advantages in terms of efficient electron transport and optical excitation, but also have the disadvantage of low surface area. Meanwhile, 2D materials exhibit large surface areas but tend to agglomerate. Interfacial engineering is a promising dimensionality-dependent technique for sustainable energy applications. A plethora of photocatalytic studies on the heterostructures of $NiTiO_3/gC_3N_4$, $NiTiO_3/TiO_2$, $Fe_2O_3/NiTiO_3$, mono/multilayer MoS_2, MoS_2 nanoflowers, 1D/2D TiO_2/MoS_2, MoS_2/graphene, Bi_2S_3/MoS_2, Au-MoS_2, $NiTiO_3/MoS_2$, phosphated 2D/3D MoS_2, CdS/MoS_2, Cu/MoS_2, and co-doped MoS_2 nanoparticles have been reported (Chang et al., 2014; Parzinger et al., 2017; Du et al., 2018; Qin et al., 2018; Li et al., 2019c; Lee et al., 2019; Lu et al., 2020; Guo et al., 2021; Khan et al., 2021; Liu et al., 2021) but to the best of our knowledge, no study on CO_2 reduction via the 1D/2D $NiTiO_3/MoS_2$ structure has been reported.

Herein, a highly synergized $NiTiO_3/MoS_2$ (1D/2D) heterostructure was synthesized using a two-step process. $NiTiO_3$ nanofibers (NFs) were firstly synthesized via electrospinning which were later combined with 2D flower-like MoS_2 via a hydrothermal process. The morphologies and optical properties of the as-synthesized photocatalysts were characterized using various techniques. The selective growth of highly reactive 1T, along with honeycomb-like 2H phases, was confirmed by X-ray photoelectron spectroscopy (XPS) and transmission electron microscopy (TEM). The hybrid $NiTiO_3/MoS_2$ exhibited a redshift to the visible light region, with enhanced absorption. At the optimum loading of MoS_2, $NiTiO_3/MoS_2$ exhibited the greatest CO_2 reduction, producing CO and CH_4 gases at 130 and 55 μmol g^{-1} h^{-1}, respectively, which are 3.8- and 3.6-times higher amounts than those (34 and 15 μmol g^{-1} h^{-1}, respectively) of pristine $NiTiO_3$ NFs, achieving an overall CO_2 selectivity of 83%. This work could contribute to the development of efficient and stable photocatalytic materials for water splitting, H_2 evolution, and other photocatalytic activities.

MATERIALS AND METHODS

Materials

All materials were of analytical grade and were used without further purification. Nickel (II) acetate tetrahydrate (98%), titanium (IV) butoxide (97%), sodium molybdate dihydrate (≥99.5%), ethanol (EtOH), and acetylacetone were purchased from Sigma–Aldrich (St. Louis, MO, United States). Polyvinylpyrrolidone K90 (MW = 360,000) and thiourea (H_2NCSNH_2), obtained from Wako Pure Chemical Industries, Ltd (Osaka, Japan), were used in the synthesis of the $NiTiO_3$ NFs. Sodium sulfate (Na_2SO_4) and triethanolamine (TEOA) from Samchun Pure Chemical Co., Ltd (Pyeongtaek-si, Korea) were used in the measurement of electrochemical and photocatalytic properties. Conductive fluorine-doped tin oxide (FTO; 15 mΩ) glass with dimensions of 2 × 6 cm^2, purchased from Korea Fine Chemical Co., Ltd., was used as a substrate film.

Preparation of $NiTiO_3$ Nanofibers

$NiTiO_3$ NFs were made via electrospinning. Briefly, titanium butoxide (2 g) was stirred in EtOH (5 ml) until it was well-mixed. Then, the required amount of nickel (II) acetate tetrahydrate was added and the solution was continuously stirred for 3 h at room temperature. Subsequently, PVP (0.6 g) was added to the solution, which was stirred continuously for another 8 h to obtain a viscous solution. Finally, acetylacetone (0.3 ml) was added and the solution was stirred for at least 2 h until uniformly light green in color. The viscosity of the solution measured using a DV2TLVCJ0 viscometer (AMETEK Brookfield, Chandler, AZ, United States) was 195 ± 5 cP. This solution was taken-up in a 12-ml nonpyrogenic plastic syringe and connected to a 25-gauge (0.26 mm) stainless-steel needle for electrospinning. The syringe was then mounted vertically and attached to a pump that was connected to a high-voltage power

supply. The distance from the needle to the collection plate was fixed at 110 mm and the flow rate was maintained at 10 μl/min. Electrospinning was performed using an electrospinning machine (Model ESR100D; NanoNC, Seoul, Korea) and maintained at 10 kV for the synthesis of $NiTiO_3$ NFs. The NFs were collected every 2 h and kept in an oven at 60°C, to remove residual solvent before heat treatment in a box furnace under an air atmosphere of 600°C (4 h, 10°C/min). These NFs were characterized without further treatment.

Preparation of $NiTiO_3/MoS_2$ Structures

$NiTiO_3/MoS_2$ with different loading amounts of MoS_2 precursors was synthesized by a hydrothermal process. The required amounts of sodium molybdate dihydrate and thiourea were dissolved in 60 ml of deionized (DI) water under stirring for 1 h. Then, 100 mg of $NiTiO_3$ NFs were added and mixed by a high-speed ultrasonic processor (VCX-130; Young Jin Corporation, Korea) for 15 min (70 rpm, 30-s pulse) to ensure uniform and complete mixing. The solution was then transferred to a 100-ml Teflon-lined autoclave to grow MoS_2 nanosheets over the $NiTiO_3$ NFs via a hydrothermal method. This mixture was maintained at 200°C for 24 h in a box furnace under an air atmosphere. Finally, the $NiTiO_3/MoS_2$ sample was collected and washed three times with DI water and EtOH to remove organic impurities. The obtained black-colored $NiTiO_3/MoS_2$ samples were dried overnight in a vacuum oven at 60°C and then characterized. **Scheme 1** illustrates the complete synthesis process. The amount of MoS_2 precursor was varied and samples were classified as NMS-01, NMS-02, NMS-03, or NMS-04 (**Supplementary Table S1**). For comparison, pristine MoS_2 was synthesized under the same process conditions without adding $NiTiO_3$ NFs.

Photoelectrochemical Performance

A three-electrode quartz cell with a potentiostat (VersaSTAT 4; Princeton Applied Research, Princeton, NJ, United States) was used to measure the photoelectrochemical performances of the photocatalysts. Electrolyte (0.5 M Na_2SO_4) was used during this process. Each photocatalyst (200 mg) was dissolved in 1.5 ml of EtOH and coated on the 2 × 4 cm^2 area of the FTO film (2 × 6 cm^2) via spin-coating at 2,500 rpm for 60 s. The as-prepared films were sintered at 150°C for 1 h to remove residual EtOH. Each coated FTO film contained ~1.5 mg of the photocatalyst. The FTO film, Pt wire, and Ag/AgCl were used as the working, counter, and reference electrodes, respectively. The films were characterized using electrochemical impedance spectroscopy (EIS) under ultraviolet-visible (UV-vis) light irradiation at frequencies ranging from 10^5 to 0.1 Hz, at an AC amplitude of 10 mV. The photocurrent density was measured while 1 V bias potential was applied via the reference electrode. All photoelectrochemical analyses were conducted using a 300-W Xe lamp (66984; Newport, Irvine, CA, United States) under UV-vis light irradiation.

Photocatalytic Activity

The photocatalytic performance of all samples was measured according to the photoreduction of CO_2 under UV-vis light irradiation. The experiments were carried out in a homemade

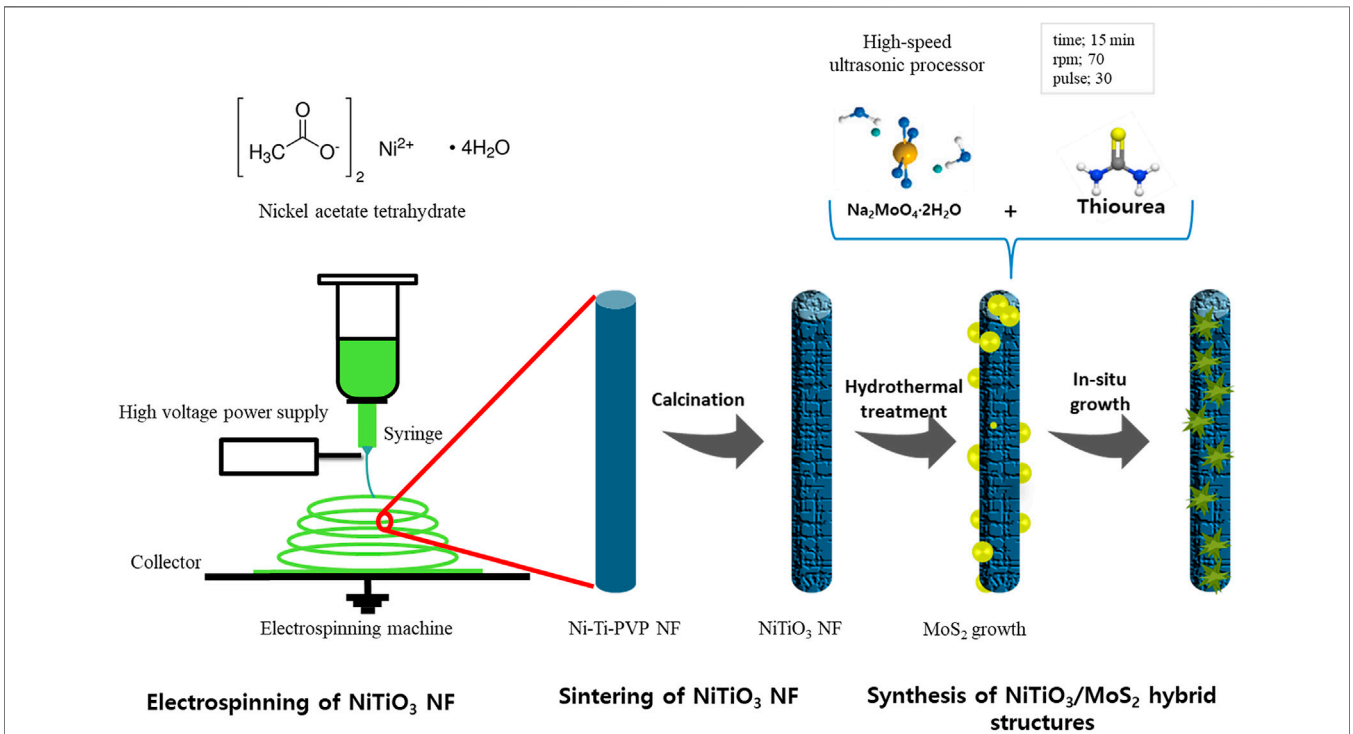

SCHEME 1 | Illustration of the complete fabrication processes of $NiTiO_3$ NFs and $NiTiO_3/MoS_2$ hybrid structures.

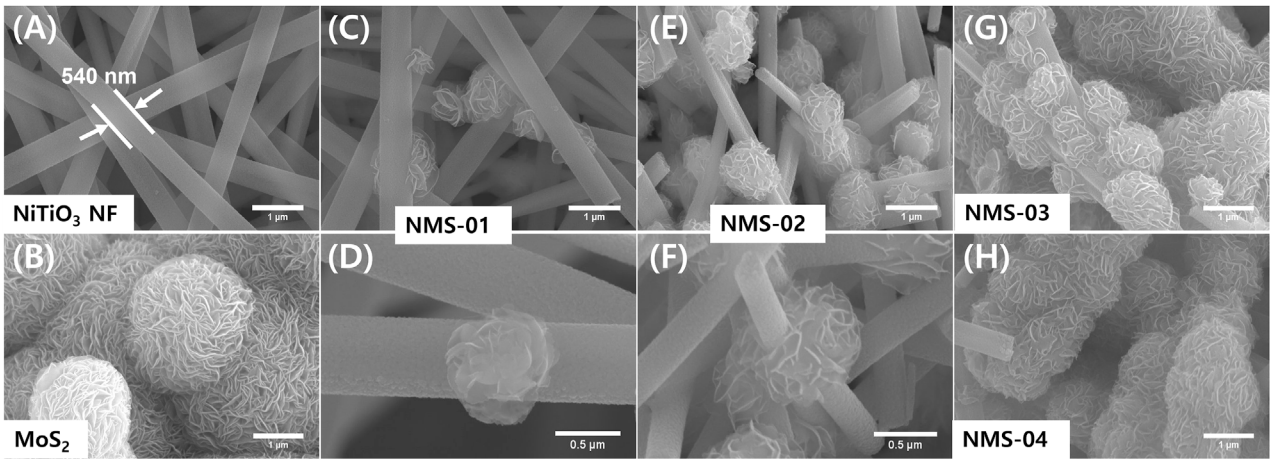

FIGURE 1 | Field-emission electron microscopy images of microstructures. **(A)** Pristine $NiTiO_3$ nanofibers, **(B)** pristine MoS_2, **(C)** low and **(D)** high magnification images of NMS-01, **(E)** low and **(F)** high magnification images of NMS-02, **(G)** agglomerated MoS_2 in NMS-03, and **(H)** NMS-04.

chemical-resistant quartz-windowed stainless-steel reactor cell (260 ml) equipped with a 300-W Xe lamp as the light source. In a typical procedure, the required amount of sample was coated on the FTO film and used as a photocatalyst to react with CO_2 and water (125 ml) inside the reactor. Triethanolamine (10 vol%) was used as a hole scavenger. Before photocatalytic experiments, the reactor cell was purged with CO_2 gas (99.99% purity; 2 bars for 2 h) to remove air and other gases. Evolved gases were collected every hour and separated by a fused silica capillary column equipped with a pulsed discharge detector (6500 GC; YL Instruments, Gyeonggi-do, Republic of Korea). Helium continuously flowed as carrier gas. A 300-W Xe lamp was used as a simulated sunlight source and the focused light intensity (10 mW cm^{-2}) was measured using an 843-R USB power meter (MKS; Newport).

Physicochemical Characterization

The microstructures of pristine $NiTiO_3$ NFs, MoS_2, and $NiTiO_3/MoS_2$ (NMS-X, where X = 1–4) were measured by field-emission scanning electron microscopy (FE-SEM; S4800; Hitachi, Japan) at 15 kV. To further investigate the structure and interaction between $NiTiO_3$ NFs and MoS_2, scanning TEM (STEM; JEM2100F; JEOL, Tokyo, Japan) analysis was performed at 200 kV. X-ray diffraction (XRD; D/Max-2500/PC; Rigaku, Tokyo, Japan) was carried out using a Bruker Advanced X-ray instrument with Cu Kα radiation at a wavelength of 1.5418 Å, to analyze the crystalline phases of the samples. A Brunauer–Emmett–Teller (BET) N_2 adsorption/desorption analyzer (TriStar II 3020; Micromeritics, Norcross, GA, United States) was used to measure the specific surface area and pore size distribution of the catalysts. To study the chemical properties of the photocatalysts, XPS (Thermo Fisher Scientific, Waltham, MA, United States) with an Al Kα source was used. Optical properties were measured by UV-vis spectroscopy (V750; JASCO, Tokyo, Japan). Fourier transform infrared spectroscopy (FTIR, iS10; Thermo Fisher Scientific) was used to confirm the presence of specific surface groups (NH_2, OH) in $NiTiO_3$ NF and NMS-02. A photoluminescence spectrophotometer (LabRAM HR-800; Horiba, Piscataway, NJ, United States) was used to study the recombination rates of the charge carriers. Contact angles (CAs) were measured at room temperature (22–25°C) and 20–30% RH using a static CA analyzer (Phoenix 300; SEO, Suwon, Republic of Korea). For the analysis, 3.4 µl of DI water was used.

RESULTS AND DISCUSSION

Field-Emission Scanning Electron Microscopy

The morphological properties of the as-prepared samples were analyzed by FE-SEM **(Figure 1)**. The pristine $NiTiO_3$ NFs **(Figure 1A)** had a smooth surface, with an average diameter of 540 nm and average length of a few micrometers. Pristine MoS_2 had a petal-like hierarchical architecture **(Figure 1B)**. Hybrid structures ($NiTiO_3/MoS_2$) were synthesized via a hydrothermal method, by varying the loading amount of MoS_2 precursors. Consequently, the hybrid structures appeared as high aspect ratio $NiTiO_3$ NFs of uniform diameter, covered by flower-like MoS_2 particles formed by sulfurization of MoO_3. Loading amounts of MoS_2 were varied and the corresponding hybrid structures were assigned the names NMS-01, NMS-02, NMS-03, and NMS-04, respectively. Growth of flower-like MoS_2 increased with increasing amounts of MoS_2 precursor. Optimal growth was observed for NMS-02 **(Figures 1E,F)**; higher loadings of MoS_2 in NMS-03 and NMS-04 resulted in agglomeration **(Figures 1G,H)**.

Transmission Electron Microscopy

To further investigate the microstructure, TEM analyses were performed on pristine $NiTiO_3$ NFs and the optimum hybrid

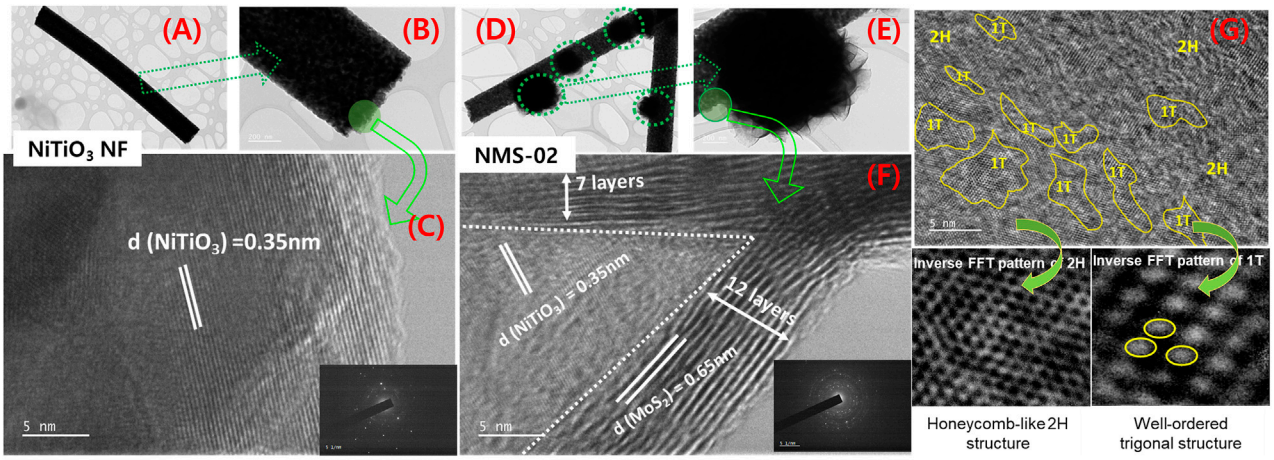

FIGURE 2 | Transmission electron microscope images of microstructures. Pristine $NiTiO_3$ nanofibers at **(A,B)** low and **(C)** high resolution indicating interplanar d-spacing, NMS-02 hybrid structure at **(D,E)** low and **(F)** high resolution showing interplanar d-spacings and the number of layers of MoS_2, and **(G)** inverse fast Fourier transform patterns revealing the co-existence of honeycomb-like 2H and well-ordered trigonal structures in the NMS-02 hybrid structure.

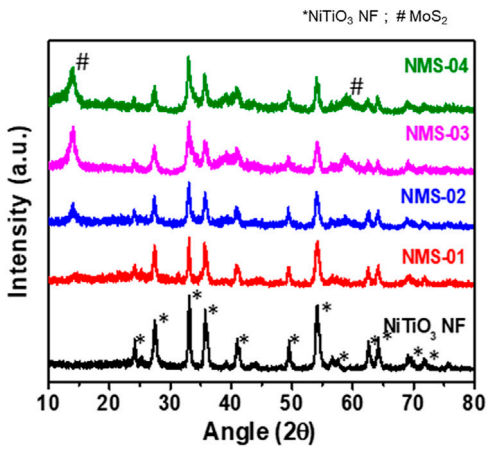

FIGURE 3 | X-ray diffraction patterns of pristine $NiTiO_3$ nanofibers and $NiTiO_3/MoS_2$ hybrid structures (NMS-01, NMS-02, NMS-03, and NMS-04).

sample (NMS-02). Low-magnification TEM images **(Figures 2A,B)** revealed the uniform size and long length of the pristine NFs. Characteristic interplanar spacing of 0.35 nm was confirmed by a high-magnification image of $NiTiO_3$ NFs **(Figure 2C)**. Low-magnification images of NMS-02 **(Figures 2D,E)** show growth of flower-like MoS_2 firmly attached to the $NiTiO_3$ NF substrate. The high-resolution TEM image **(Figure 2F)** shows lattice fringes of $NiTiO_3$ NFs and MoS_2 with d-spacings of 0.35 and 0.65 nm, respectively, indicating intimate interfacial contact. Layers (7–12) of MoS_2 covered the $NiTiO_3$ NFs. This analysis confirmed the successful formation of a 1D/2D ($NiTiO_3/MoS_2$) hybrid structure. High-resolution TEM images confirmed the coexistence of honeycomb-like 2H and well-ordered trigonal 1T phases. The 1T/2H hybrid structure was directly observed via selected area inverse fast Fourier transform (FTT) **(Figure 2G)**. Insertion of the 1T (metallic) phase into the 2H phase (semiconductor) enhanced the catalytically active site in the composite structure.

X-ray Diffraction

The phase structures of the samples were characterized by X-ray diffraction (**Figure 3**). Pristine $NiTiO_3$ showed characteristic peaks at 2θ = 24.09°, 33.06°, 35.73°, 40.96°, 49.40°, 54.08°, 62.45°, 64.03°, and 71° that were assigned to the (012), (104), (110), (113), (024), (116), (124), (300), and (1010) planes of $NiTiO_3$ NFs (JCPDS No. 01-076-0334). In addition to the intense peaks of the $NiTiO_3$ NFs, a peak due to rutile TiO_2 appeared at 27.37° (JCPDS No. 98-000-0375). All hybrid samples contained some additional peaks at 2θ = 14.1°, 39.41°, and 58.69°, which were attributed to the (002), (103), and (110) planes of MoS_2 (JCPDS 01-075-1539). The presence of all characteristic peaks of $NiTiO_3$ NFs and MoS_2 in the XRD spectra of the composite samples confirmed successful integration of the $NiTiO_3/MoS_2$ hybrid structure, in agreement with the TEM results.

X-ray Photoelectron Spectroscopy

XPS was performed to investigate the chemical composition and effect of MoS_2 loading on the $NiTiO_3$ NFs **(Figure 4)**. Survey spectra **(Figure 4A)** confirmed the presence of all essential elements (Ni, Ti, O, Mo, and S) in the $NiTiO_3/MoS_2$ hybrid structure, in correspondence with SEM mapping results **(Supplementary Figure S3)**. The NMS-02 spectra were further analyzed to investigate the chemical states and interaction between $NiTiO_3$ and MoS_2. The Mo 3d signal **(Figure 4B)** consisted of two prominent peaks related to Mo^{4+}. High-intensity peaks at 229.3 and 232.4 eV, corresponding to Mo^{4+} $3d_{5/2}$ and Mo^{4+} $3d_{3/2}$, respectively, were attributed to the 1T MoS_2 phase; two other peaks at 230.1 and 233.3 eV were assigned to the 2H phases of MoS_2. A pair of peaks at 234.2 and 236.0 eV were attributed to Mo^{6+} of MoO_3. One additional peak at 226.4 eV was assigned to S 2s. The S 2p spectrum **(Figure 4C)** was deconvoluted into four peaks having energies of 162.0, 162.7,

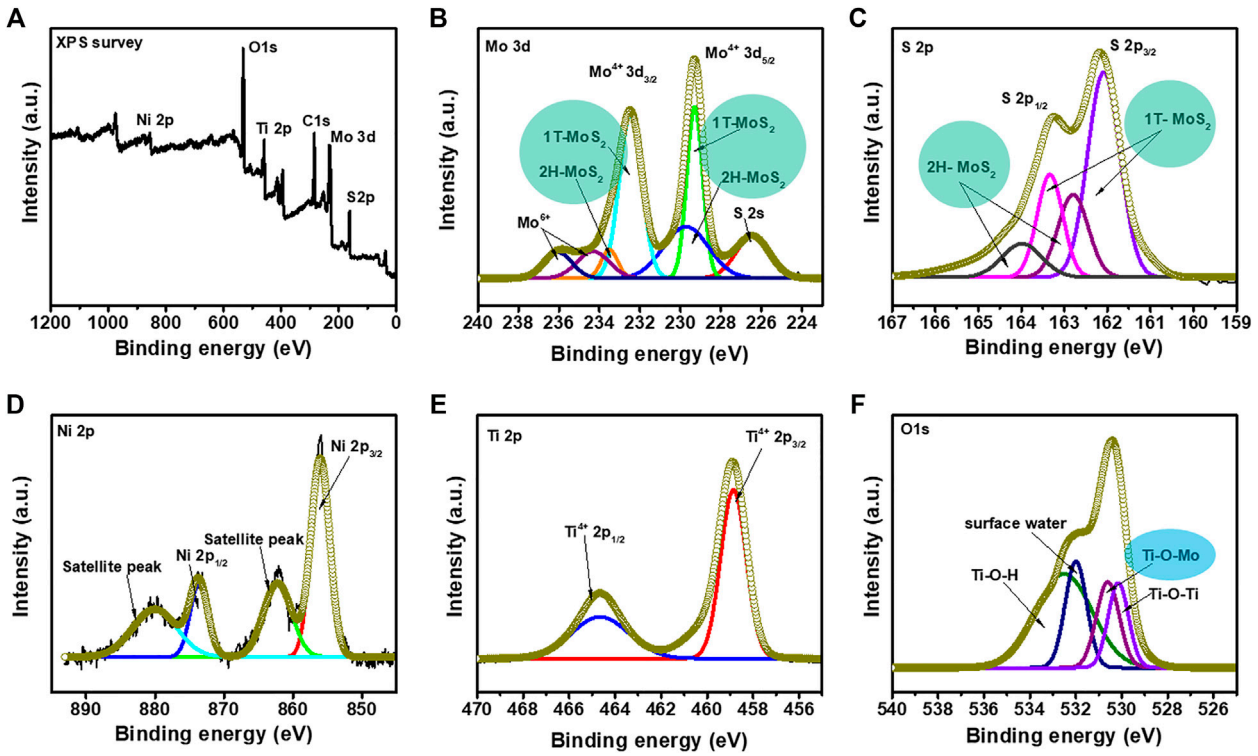

FIGURE 4 | X-ray photoelectron spectra of NMS-2 **(A)** Survey spectrum. Deconvoluted spectra of **(B)** Mo 3d band showing characteristic peaks of the 1T and 2H MoS_2 phases **(C)** S 2p band showing characteristic peaks of the 1T and 2H phases of MoS_2, **(D)** Ni 2p band **(E)** Ti 2p band, and **(F)** O 1s band confirming strong interaction between the $NiTiO_3$ nanofibers and MoS_2 constituents in the hybrid structure.

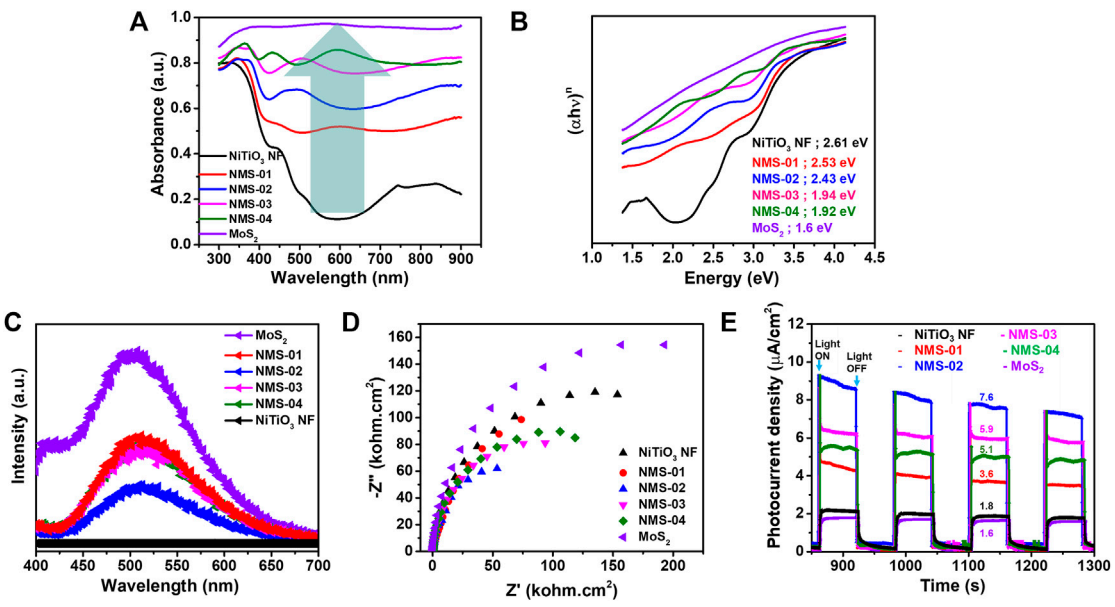

FIGURE 5 | (A) Ultraviolet-visible light absorption **(B)** bandgap energy, **(C)** photoluminescence, and **(D)** electrochemical impedance spectra expressed as Nyquist plots, **(E)** photocurrent density measurements for the pristine $NiTiO_3$ nanofibers and various hybrid structures.

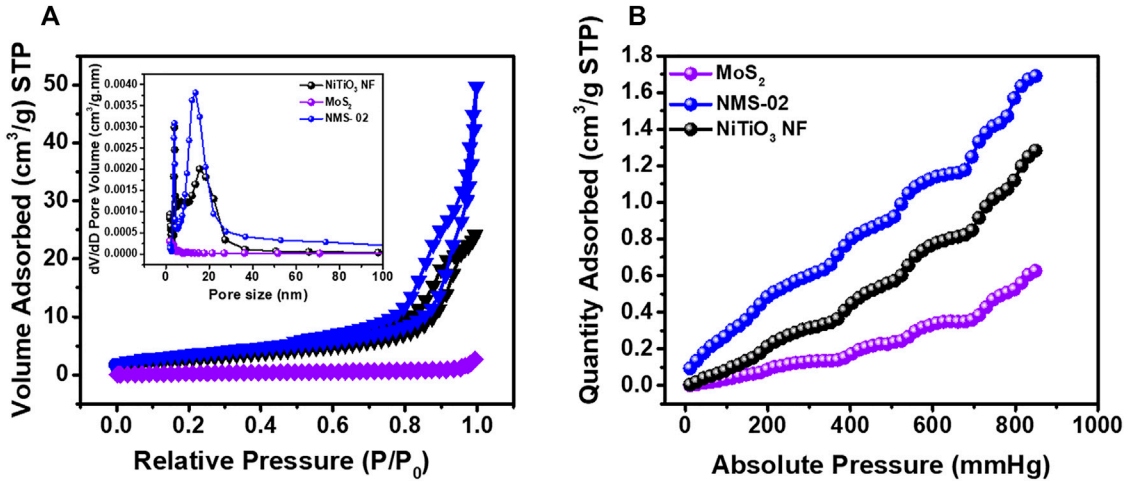

FIGURE 6 | (A) Brunauer–Emmett–Teller nitrogen adsorption-desorption isotherms at 77 K. Inset shows the Barrett–Joyner–Halenda pore size distribution. **(B)** CO_2 adsorption isotherms at 298 K for pristine $NiTiO_3$ NF, MoS_2, and NMS-02 photocatalysts degassed overnight at 100°C.

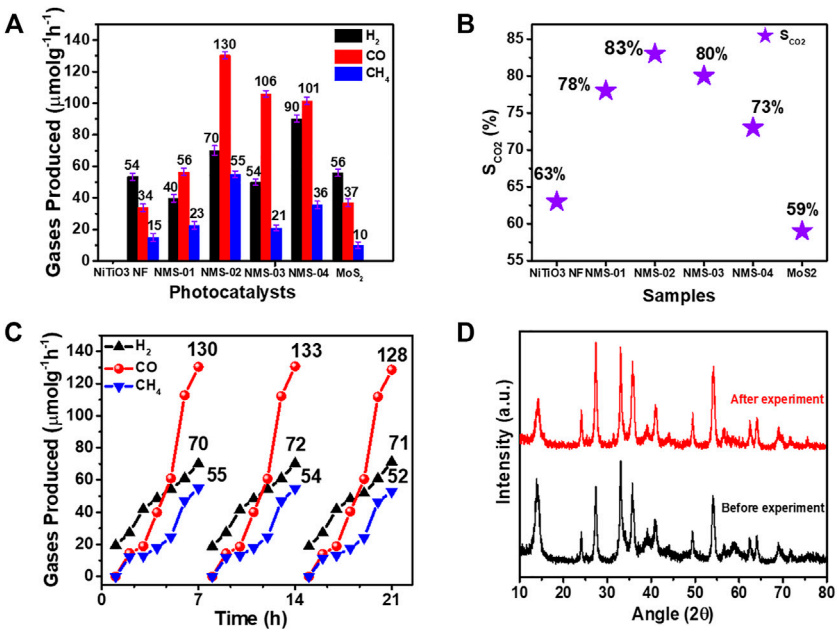

FIGURE 7 | Photocatalytic CO_2 reduction performance of as-prepared samples. **(A)** Yields of the gases produced. **(B)** Comparison of CO_2 selectivity among the samples **(C)** Stability test results of the optimum sample (NMS-02).) **(D)** XRD analysis of NMS-02 after the stability test.

163.3, and 164.1 eV. Peaks at 162.0 and 163.3 eV corresponding to S $2p_{3/2}$ and S $2p_{1/2}$ were attributed to 1T-MoS_2 while the peaks at 162.7 and 164.1 eV corresponding to S $2p_{3/2}$ and S $2p_{1/2}$, respectively, were attributed to 2H-MoS_2. The Ni 2p spectrum was deconvoluted into two major peaks corresponding to Ni $3p_{3/2}$ and Ni $2p_{1/2}$ at 855.9 and 873.7 eV, respectively **(Figure 4D)**. Peaks in the Ti 2p spectra appearing at 458.8 and 464.6 eV were assigned to Ti $2p_{2/3}$ and Ti $2p_{1/2}$, respectively **(Figure 4E)**. Four O 1s peaks **(Figure 4F)** at 530.1, 530.6, 531.9, and 532.5 eV were attributed to Ti–O–Ti, Ti–O–Mo, surface water, and Ti–O–H bonds, respectively. The appearance of the peak at 530.6 eV due to the Ti–O–Mo linkage indicated a strong chemical interaction between $NiTiO_3$ and MoS_2 in $NiTiO_3/MoS_2$, which could improve photocatalytic activity.

Optical Properties

The optical properties of the as-prepared samples were measured by UV-vis spectroscopy over the range of 300–900 nm **(Figure 5A)**. Pristine $NiTiO_3$ NFs displayed an absorption edge of 474 nm with little light absorption, especially in the

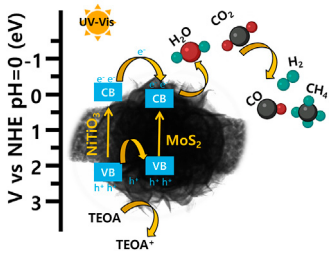

FIGURE 8 | Schematic illustration of the proposed charge transfer mechanism for CO_2 photoreduction under ultraviolet-visible light illumination on $NiTiO_3/MoS_2$ photocatalyst.

visible region. The light absorption edge red-shifted from 489 nm (NMS-01) to 636 nm (NMS-04) with increasing loading of MoS_2 onto the $NiTiO_3$ NFs. The optimum sample (NMS-02), with an absorption edge of 509 nm, showed more light absorption than pristine $NiTiO_3$ NFs, confirming the structural advantage of the composite sample. This enhanced UV-Vis light absorption could promote photocatalytic activity. The bandgap energies estimated using the Tauc method **(Figure 5B)** were 2.61, 2.53, 2.43, 1.94, 1.92, and 1.6 eV for $NiTiO_3$ NF, NMS-01, NMS-02, NMS-03, NMS-04, and pristine MoS_2 photocatalysts, respectively. This steady reduction in bandgap energy was attributed to the inherent light absorption of the black MoS_2.

Photoluminescence and Photoelectrochemical Performance

For a photocatalyst to show high performance, low rates of recombination of the charge carriers are crucial. Photoluminescence analysis was performed at an excitation wavelength of 325 nm to study the effect of MoS_2 loading on charge carrier recombination, to design an efficient heterostructure **(Figure 5C)**. Pristine $NiTiO_3$ NFs showed no intense peaks, which indicated no activation in this region, while MoS_2 showed high PL intensity due to high recombination rates. A remarkable reduction in charge carrier recombination was found, reflected in quenching of PL peak intensity when MoS_2 was added to the $NiTiO_3$ NFs. The lowest peak intensity for NMS-02 indicated the significance of identifying the optimum amount of MoS_2, to design an efficient heterostructure to restrain charge carrier recombination. The decreased PL intensity for NMS-02 relative to all of the other photocatalysts was reflected in the highest photocatalytic performance. We performed EIS analysis under UV-vis irradiation to confirm the results obtained by PL spectroscopy, and to study the nature of the charge **(Figure 5D)**. A smaller semicircle radius in a Nyquist plot represents lower recombination and more efficient charge transfer across an interface. All of the composite samples showed smaller radii compared with the pristine samples, which confirmed that the growth of MoS_2 on $NiTiO_3$ NFs promoted successful electron transfer, resulting in enhanced photocatalytic performance. The radius was smallest for NMS-02, which also corroborated that it had the best CO_2 reduction performance. To further confirm its effectiveness of the 1D/2D hybrid structure on the separation of photogenerated electrons and holes, transient photocurrent intensities were measured for bare and hybrid catalysts **(Figure 5E)**. The transient photocurrent was measured while switching the light on and off after every 60 s. The photocurrent density of pristine $NiTiO_3$ NF and MoS_2 showed the lowest values of 1.6 $\mu A/cm^2$, and 1.8 $\mu A/cm^2$ respectively while the hybrid structures NMS-01, NMS-02, NMS-03, and NMS-04 showed 3.6 $\mu A/cm^2$, 7.6 $\mu A/cm^2$, 5.9 $\mu A/cm^2$, and 3.6 $\mu A/cm^2$ respectively. This increase in the photocurrent density observed in the hybrid structures, is attributed to the successful formation of heterostructure between 1D $NiTiO_3$ NFs and 2D MoS_2 nanosheets.

Surface Area and Pore Size Distribution

Nitrogen adsorption-desorption BET isotherms and Barrett–Joyner–Halenda (BJH) pore size distributions were determined to further investigate the microstructures **(Figure 6)**. All samples were degassed overnight at 100°C prior to analysis. The N_2 isotherms **(Figure 6A)** for MoS_2 had the smallest specific surface area due to highly densely clustered nanosheets. However, when MoS_2 sheets were grown on the $NiTiO_3$ NFs, the specific surface area significantly increased due to hierarchical "puffy" nanosheets of MoS_2 dispersed over the surface of the NFs. The higher specific surface area of the composite structure could provide more adsorption and reactive sites, to enhance photocatalytic performance. The BJH pore size distribution plots **(Figure 6A**, inset**)** show typical adsorption-desorption isotherms for $NiTiO_3$ and NMS-02 hybrid structures that confirmed the presence of pores, while the isotherms for pristine MoS_2 indicated the absence of pores. This analysis showed that porous $NiTiO_3$ NFs favored the growth of structurally stable vertical nanosheets of MoS_2. The reduction of CO_2 in the presence of water is usually in fierce competition with hydrogen evolution reaction (HER). This causes low activity and selectivity toward CO_2 photoreduction. Therefore, the adsorption and activation of the CO_2 on the surface of the catalyst are crucial for the subsequent reduction process. The amounts of CO_2 adsorbed for the TiO_2 NF, NMS-02, and MoS-02 were analyzed at 25°C **(Figure 6B)**. Results show a higher amount of CO_2 adsorption on the surface of the NMS-02 hybrid sample (1.73 cm^3/g STP) than that of pristine $NiTiO_3$ NF (1.29 cm^3/g STP) and pristine MoS_2 (0.62 cm^3/g STP). The epitaxial growth of MoS_2 combined with the porous structure of $NiTiO_3$ NFs provided more active sites for CO_2 diffusion and adsorption. FTIR analysis showed the presence of OH groups on the surface of $NiTiO_3$ NF and NMS-02 catalysts (**Supplementary Figure S4**). Surface hydroxyl (OH) and amino groups are prone to donate their protons to CO_2 to make negatively charged species which help improve CO_2 adsorption and proton production which enhances the efficiency of CO_2 photoreduction (Liu P. et al., 2020). The higher adsorption ability of the $NiTiO_3/MoS_2$ hybrid sample supported its high CO_2 reduction performance. The BET analysis results are summarized in **Supplementary Table S2**.

Photocatalytic CO_2 Photoreduction and its Mechanism

To investigate the photocatalytic performance of the samples, CO_2 photoreduction experiments were performed in a custom-made steel reactor equipped with a quartz window. A 300-W Xe lamp was used as the UV-vis light source. Three sequential experiments were performed under the same conditions to confirm the reliability of the results. Control experiments were also performed without using CO_2 and photocatalyst; no by-products were obtained, which indicated that photocatalyst and CO_2 are essential to convert CO_2 into useful hydrocarbon fuels (**Supplementary Figure S1**). **Figure 7** presents the CO_2 reduction results. Carbon monoxide was a major gas with comparatively small amounts of H_2 and CH_4 as side products. Pristine $NiTiO_3$ NF and MoS_2 showed markedly poorer yields compared with the composite samples, because of their moderate light absorption and charge separation properties. Carbon monoxide and CH_4 yields increased with increasing MoS_2 loading and reached the optimum value in NMS-02 (CO: 130 $\mu mol\, g^{-1}\, h^{-1}$; CH_4: 55 $\mu mol\, g^{-1}\, h^{-1}$). Yields decreased with further increases in MoS_2 loading to NMS-03 (CO: 106 $\mu mol\, g^{-1}\, h^{-1}$; CH_4: 21 $\mu mol\, g^{-1}\, h^{-1}$) and NMS-04 (CO: 101 $\mu mol\, g^{-1}\, h^{-1}$; CH_4: 36 $\mu mol\, g^{-1}\, h^{-1}$), which suggested that excess MoS_2 might have induced charge carrier recombination during the reaction process. The low activity of the composite samples with higher MoS_2 contents may also be partly due to fewer active sites, due to agglomerated MoS_2 sheets as observed in SEM images. The CO and CH_4 yields of the optimum sample of NMS-02 were 3.8- and 3.6-times those of pristine $NiTiO_3$ NF (34 and 15 $\mu mol\, g^{-1}\, h^{-1}$, respectively) and 3.6- and 5.5-times those of the pristine MoS_2 (37 and 10 $\mu mol\, g^{-1}\, h^{-1}$, respectively) (**Figure 7A**). The amounts of gases produced by our hybrid samples were significantly higher than those reported elsewhere for photocatalysts containing $NiTiO_3$ NFs and MoS_2 (**Supplementary Table S3**), because the epitaxial growth of MoS_2 over $NiTiO_3$ NFs enhanced light absorption and exposed active edges. Mixed (1T/2H) phases of MoS_2, enhanced CO_2 adsorption, and improved charge separation might also have contributed to the significantly higher performance of the NMS-02 photocatalyst.

$$\mathbf{S}_{CO2}\ (\%) = \frac{2\mathbf{n}_{CO} + 8\mathbf{n}_{CH4}}{2\mathbf{n}_{H2} + 2\mathbf{n}_{CO} + 8\mathbf{n}_{CH4}} \times 100 \qquad (1)$$

Hydrophobic surfaces suppress H_2 evolution, thereby favoring CO_2 photoreduction reactions by exerting an umbrella-like effect over photocatalysts to minimize water contact (Li et al., 2019a; Wakerley et al., 2019). CA measurements confirmed that the optimum sample was comparatively hydrophilic compared with pristine $NiTiO_3$ NFs and MoS_2 (**Supplementary Figure S2**). Here, hydrophobicity could have been partly induced by the presence of the semiconducting hydrophobic 2H phase, and partly by the epitaxial growth of MoS_2 over the $NiTiO_3$ NFs. Generally, 90° is considered a critical angle for distinguishing between hydrophilic (CA < 90°) and hydrophobic (CA ≥ 90°) behavior. However, in our study, surfaces with CAs close to 90° were identified as hydrophobic while those with lower CAs were deemed hydrophilic.

The CO_2 selectivity (S_{CO2}) of each catalyst can be calculated according to **Eq. 1**, where n is the amount of H_2, CO, and CH_4 produced in units of $\mu mol\, g^{-1}\, h^{-1}$ during 7 h of light irradiation. The highest selectivity, of 83%, was recorded for NMS-02, which compares with 63%, 78%, 80%, 73%, and 59% for $NiTiO_3$ NFs, NMS-01, NMS-03, NMS-04, and MoS_2, respectively **(Figure 7B)**. The stability of the optimum sample was determined by measuring CO_2 reduction performance. The experiment was repeated for up to three cycles; after each cycle, the sample was removed from the instrument, and heated at 100°C for 4 h to remove DI water and TEOA. No significant change in performance was observed during the three consecutive experiments, which indicated good photocatalyst stability **(Figure 7C)**. Moreover, the sample was collected after the completion of the stability test for XRD analysis. **Figure 7D** clearly shows that the XRD pattern before and after the CO_2 photoreduction looks almost similar. No observable change was observed according to XRD analysis, confirming that the heterostructure is highly stable.

CO_2 reduction results confirmed that pure $NiTiO_3$ NFs and pure MoS_2 showed exceptionally lower amounts of CO and CH_4 as compared to those for $NiTiO_3/MoS_2$ heterostructures. It can be inferred that the photocatalytic reduction of CO_2 can be improved by light-harvesting, photogenerated carrier generating, and the CO_2 adsorption capacity of the catalyst. Results of UV-Vis absorbance, PL, photocurrent density, and BET analysis show that the introduction of MoS_2 nanosheets on the surface of $NiTiO_3$ nanofibers can effectively increase the light absorption, charge separation, and CO_2 adsorption and activation ability of the catalyst. As the activated CO_2 is more susceptible to the reduction, the photogenerated electrons on the surface of heterostructure will react with the activated CO_2 and H_2O to form carbon-containing products as well as H_2. $NiTiO_3$ nanofibers decorated with flower-like MoS_2, improving the selectivity of the CO, and CH_4 products through the higher density of the photogenerated electrons to suppress the H_2 formation on the active sides of the heterostructure. Based on the above results and discussions, a mechanism for the CO_2 photocatalytic reduction process can be proposed in **Figure 8**. Under simulated light irradiation, photogenerated electrons are excited from the conduction band (CB) of $NiTiO_3$ NFs to the valence band (VB) of $NiTiO_3$ nanofibers from where electrons migrate to CB of the MoS_2 nanosheets due to good band alignment between the two components. Subsequently, the excited electrons from the CB of MoS_2 nanosheets react with adsorbed CO_2 and water producing CO and CH_4. Meanwhile, the holes at VB-holes move from the VB of $NiTiO_3$ NF to VB of MoS_2 where they combine with TEOA to oxidize TEOA to $TEOA^+$. The electrons enriched active sites of MoS_2 in CB would be used for CO_2 reduction. Thus, the synthesized hybrid structure delayed recombination of electron-hole pairs, thereby improving charge transfer at the interface.

CONCLUSION

Full spectrum-induced hybrid structures consisting of 1D $NiTiO_3$ decorated with 1T/2H MoS_2 were prepared via a facile one-step hydrothermal method. The key parameters for tailoring the

morphology, porosity, surface, and interfacial properties of the photocatalysts were identified, with a view to efficient and selective conversion of CO_2 into valuable chemicals. Introduction of MoS_2 layers onto the $NiTiO_3$ NFs increased the CO_2 selectivity to 83% for the optimized hybrid structure, which compares with 63% and 59% for pristine $NiTiO_3$ NFs and MoS_2, respectively. This large improvement was attributed to the positive synergistic effect between the $NiTiO_3$ NFs and MoS_2 in the hybrid photocatalyst. High CO_2 selectivity could also be attributed to enhanced light absorption, an abundance of active edges, insertion of multiphase (2H/1T) MoS_2, and higher surface area, and partly to the hydrophobic nature of the composite structure. We believe that this strategy provides a new route to the design and manufacture of more energy-efficient materials having higher photocatalytic activity.

DATA AVAILABILITY STATEMENT

The original contributions presented in the study are included in the article/**Supplementary Material**, further inquiries can be directed to the corresponding author.

AUTHOR CONTRIBUTIONS

HK conceived and performed the experiments and wrote a draft of the paper. SK helped during experiments and data analysis. HC helped during experiments and data collection while CL supervised the overall work and polished the paper. All authors have approved the final version of the article.

FUNDING

This work was supported by the Industrial Technology Innovation Program of the Korea Evaluation Institute of Industrial Technology (KIET) provided financial resources from the Ministry of Trade, Industry & Energy, Republic of Korea (No. 20012211).

SUPPLEMENTARY MATERIAL

The Supplementary Material for this article can be found online at: https://www.frontiersin.org/articles/10.3389/fchem.2022.837915/full#supplementary-material

REFERENCES

Asadi, M., Kumar, B., Behranginia, A., Rosen, B. A., Baskin, A., Repnin, N., et al. (2014). Robust Carbon Dioxide Reduction on Molybdenum Disulphide Edges. *Nat. Commun.* 5, 1–8. doi:10.1038/ncomms5470

Chang, K., Mei, Z., Wang, T., Kang, Q., Ouyang, S., and Ye, J. (2014). MoS2/Graphene Cocatalyst for Efficient Photocatalytic H2 Evolution under Visible Light Irradiation. *ACS Nano* 8, 7078–7087. doi:10.1021/nn5019945

Chen, Y., Jia, G., Hu, Y., Fan, G., Tsang, Y. H., Li, Z., et al. (2017). Two-dimensional Nanomaterials for Photocatalytic CO2reduction to Solar Fuels. *Sustain. Energ. Fuels* 1, 1875–1898. doi:10.1039/c7se00344g

Du, J., Wang, H., Yang, M., Zhang, F., Wu, H., Cheng, X., et al. (2018). Highly Efficient Hydrogen Evolution Catalysis Based on MoS 2/CdS/TiO 2 Porous Composites. *Int. J. Hydrogen Energ.* 43, 9307–9315. doi:10.1016/j.ijhydene.2018.03.208

Gan, X., Lei, D., Ye, R., Zhao, H., and Wong, K.-Y. (2021). Transition Metal Dichalcogenide-Based Mixed-Dimensional Heterostructures for Visible-Light-Driven Photocatalysis: Dimensionality and Interface Engineering. *Nano Res.* 14, 2003–2022. doi:10.1007/s12274-020-2955-x

Guo, H., Wan, S., Wang, Y., Ma, W., Zhong, Q., and Ding, J. (2021). Enhanced Photocatalytic CO2 Reduction over Direct Z-Scheme NiTiO3/g-C3n4 Nanocomposite Promoted by Efficient Interfacial Charge Transfer. *Chem. Eng. J.* 412, 128646. doi:10.1016/j.cej.2021.128646

He, H., Lin, J., Fu, W., Wang, X., Wang, H., Zeng, Q., et al. (2016). MoS2/TiO2Edge-On Heterostructure for Efficient Photocatalytic Hydrogen Evolution. *Adv. Energ. Mater.* 6, 1600464–1600467. doi:10.1002/aenm.201600464

Khan, H., Kang, S., and Lee, C. S. (2021). Evaluation of Efficient and Noble-Metal-Free NiTiO3 Nanofibers Sensitized with Porous gC3N4 Sheets for Photocatalytic Applications. *Catalysts* 11, 385–416. doi:10.3390/catal11030385

Lee, H. I., Yu, H., Rhee, C. K., and Sohn, Y. (2019). Electrochemical Hydrogen Evolution and CO2 Reduction over Hierarchical MoSxSe2-X Hybrid Nanostructures. *Appl. Surf. Sci.* 489, 976–982. doi:10.1016/j.apsusc.2019.06.002

Li, A., Cao, Q., Zhou, G., Schmidt, B. V. K. J., Zhu, W., Yuan, X., et al. (2019a). Three-Phase Photocatalysis for the Enhanced Selectivity and Activity of CO 2 Reduction on a Hydrophobic Surface. *Angew. Chem.* 131, 14691–14697. doi:10.1002/ange.201908058

Li, H., Wang, G., Gong, H., and Jin, Z. (2020a). Phosphated 2D MoS 2 Nanosheets and 3D NiTiO 3 Nanorods for Efficient Photocatalytic Hydrogen Evolution. *ChemCatChem* 12, 5492–5503. doi:10.1002/cctc.202000903

Li, S., Chen, J., Hu, S., Wang, H., Jiang, W., and Chen, X. (2020b). Facile Construction of Novel Bi2WO6/Ta3N5 Z-Scheme Heterojunction Nanofibers for Efficient Degradation of Harmful Pharmaceutical Pollutants. *Chem. Eng. J.* 402, 126165. doi:10.1016/j.cej.2020.126165

Li, S., Wang, C., Cai, M., Yang, F., Liu, Y., Chen, J., et al. (2022a). Facile Fabrication of TaON/Bi2MoO6 Core-Shell S-Scheme Heterojunction Nanofibers for Boosting Visible-Light Catalytic Levofloxacin Degradation and Cr(VI) Reduction. *Chem. Eng. J.* 428, 131158. doi:10.1016/j.cej.2021.131158

Li, S., Wang, C., Liu, Y., Cai, M., Wang, Y., Zhang, H., et al. (2022b). Photocatalytic Degradation of Tetracycline Antibiotic by a Novel Bi2Sn2O7/Bi2MoO6 S-Scheme Heterojunction: Performance, Mechanism Insight and Toxicity Assessment. *Chem. Eng. J.* 429, 132519. doi:10.1016/j.cej.2021.132519

Li, S., Wang, C., Liu, Y., Xue, B., Jiang, W., Liu, Y., et al. (2021). Photocatalytic Degradation of Antibiotics Using a Novel Ag/Ag2S/Bi2MoO6 Plasmonic P-N Heterojunction Photocatalyst: Mineralization Activity, Degradation Pathways and Boosted Charge Separation Mechanism. *Chem. Eng. J.* 415, 128991. doi:10.1016/j.cej.2021.128991

Li, X., Yu, J., Jaroniec, M., and Chen, X. (2019b). Cocatalysts for Selective Photoreduction of CO2 into Solar Fuels. *Chem. Rev.* 119, 3962–4179. doi:10.1021/acs.chemrev.8b00400

Li, Y., Xu, J., Peng, M., Liu, Z., Li, X., and Zhao, S. (2019c). MoS2/NiTiO3 Heterojunctions as Photocatalysts: Improved Charge Separation for Promoting Photocatalytic Hydrogen Production Activity. *Catal. Surv. Asia* 23, 277–289. doi:10.1007/s10563-019-09282-4

Li, Z., Meng, X., and Zhang, Z. (2018). Recent Development on MoS2-Based Photocatalysis: A Review. *J. Photochem. Photobiol. C: Photochem. Rev.* 35, 39–55. doi:10.1016/j.jphotochemrev.2017.12.002

Liu, H., Wu, R., Zhang, H., and Ma, M. (2020a). Microwave Hydrothermal Synthesis of 1T@2H–MoS 2 as an Excellent Photocatalyst. *ChemCatChem* 12, 893–902. doi:10.1002/cctc.201901569

Liu, J., Li, X., Han, C., Zhou, X., Li, X., Liang, Y., et al. (2021). Ternary NiTiO3@g-C3n4-Au Nanofibers with a Synergistic Z-Scheme Core@shell Interface and Dispersive Schottky Contact Surface for Enhanced Solar Photocatalytic Activity. *Mater. Chem. Front.* 5, 2730–2741. doi:10.1039/d0qm00954g

Liu, P., Peng, X., Men, Y.-L., and Pan, Y.-X. (2020b). Recent Progresses on Improving CO2 Adsorption and Proton Production for Enhancing Efficiency of Photocatalytic CO2 Reduction by H2O. *Green. Chem. Eng.* 1, 33–39. doi:10.1016/j.gce.2020.09.003

Lu, J., Zhang, Z., Cheng, L., and Liu, H. (2020). MoS2-wrapped Mn0.2Cd0.8S Nanospheres towards Efficient Photocatalytic H2 Generation and CO2 Reduction. *New J. Chem.* 44, 13728–13737. doi:10.1039/d0nj02174a

Parzinger, E., Mitterreiter, E., Stelzer, M., Kreupl, F., Ager, J. W., Holleitner, A. W., et al. (2017). Hydrogen Evolution Activity of Individual Mono-, Bi-, and Few-Layer MoS 2 towards Photocatalysis. *Appl. Mater. Today* 8, 132–140. doi:10.1016/j.apmt.2017.04.007

Peng, W., Li, Y., Zhang, F., Zhang, G., and Fan, X. (2017). Roles of Two-Dimensional Transition Metal Dichalcogenides as Cocatalysts in Photocatalytic Hydrogen Evolution and Environmental Remediation. *Ind. Eng. Chem. Res.* 56, 4611–4626. doi:10.1021/acs.iecr.7b00371

Pham, T.-T., and Shin, E. W. (2020). Inhibition of Charge Recombination of NiTiO3 Photocatalyst by the Combination of Mo-Doped Impurity State and Z-Scheme Charge Transfer. *Appl. Surf. Sci.* 501, 143992. doi:10.1016/j.apsusc.2019.143992

Qin, H., Guo, R.-T., Liu, X.-Y., Pan, W.-G., Wang, Z.-Y., Shi, X., et al. (2018). Z-scheme MoS2/g-C3n4 Heterojunction for Efficient Visible Light Photocatalytic CO2 Reduction. *Dalton Trans.* 47, 15155–15163. doi:10.1039/c8dt02901f

Qu, X., Liu, M., Zhang, W., Sun, Z., Meng, W., Shi, L., et al. (2020). A Facile Route to Construct NiTiO3/Bi4NbO8Cl Heterostructures for Enhanced Photocatalytic Water Purification. *J. Mater. Sci.* 55, 9330–9342. doi:10.1007/s10853-020-04664-w

Su, T., Shao, Q., Qin, Z., Guo, Z., and Wu, Z. (2018). Role of Interfaces in Two-Dimensional Photocatalyst for Water Splitting. *ACS Catal.* 8, 2253–2276. doi:10.1021/acscatal.7b03437

Thomas, N., Mathew, S., Nair, K. M., O'Dowd, K., Forouzandeh, P., Goswami, A., et al. (2021). 2D MoS2: Structure, Mechanisms, and Photocatalytic Applications. *Mater. Today SustainabilityToday Sustain* 13, 100073. doi:10.1016/j.mtsust.2021.100073

Thompson, W. A., Sanchez Fernandez, E., and Maroto-Valer, M. M. (2020). Review and Analysis of CO2 Photoreduction Kinetics. *ACS Sustain. Chem. Eng.* 8, 4677–4692. doi:10.1021/acssuschemeng.9b06170

Wakerley, D., Lamaison, S., Ozanam, F., Menguy, N., Mercier, D., Marcus, P., et al. (2019). Bio-inspired Hydrophobicity Promotes CO2 Reduction on a Cu Surface. *Nat. Mater.* 18, 1222–1227. doi:10.1038/s41563-019-0445-x

Wang, C., Cai, M., Liu, Y., Yang, F., Zhang, H., Liu, J., et al. (2022). Facile Construction of Novel Organic-Inorganic Tetra (4-carboxyphenyl) porphyrin/Bi2MoO6 Heterojunction for Tetracycline Degradation: Performance, Degradation Pathways, Intermediate Toxicity Analysis and Mechanism Insight. *J. Colloid Interf. Sci.* 605, 727–740. doi:10.1016/j.jcis.2021.07.137

Xu, F., Zhu, B., Cheng, B., Yu, J., and Xu, J. (2018). 1D/2D TiO 2/MoS 2 Hybrid Nanostructures for Enhanced Photocatalytic CO 2 Reduction. *Adv. Opt. Mater.* 6, 1800911–1800915. doi:10.1002/adom.201800911

Zeng, S., Kar, P., Thakur, U. K., and Shankar, K. (2018). A Review on Photocatalytic CO2reduction Using Perovskite Oxide Nanomaterials. *Nanotechnology* 29, 052001. doi:10.1088/1361-6528/aa9fb1

Zhang, X., Teng, S. Y., Loy, A. C. M., How, B. S., Leong, W. D., and Tao, X. (2020). Transition Metal Dichalcogenides for the Application of Pollution Reduction: A Review. *Nanomaterials* 10, 1012. doi:10.3390/nano10061012

Conflict of Interest: Author SK was employed by Pohang Iron and Steel Co., Ltd.

The remaining authors declare that the research was conducted in the absence of any commercial or financial relationships that could be construed as a potential conflict of interest.

Publisher's Note: All claims expressed in this article are solely those of the authors and do not necessarily represent those of their affiliated organizations, or those of the publisher, the editors and the reviewers. Any product that may be evaluated in this article, or claim that may be made by its manufacturer, is not guaranteed or endorsed by the publisher.